Article

Functionalized Graphene Derivatives and TiO$_2$ for High Visible Light Photodegradation of Azo Dyes

Álvaro Pérez-Molina, Sergio Morales-Torres[ID], Francisco J. Maldonado-Hódar[ID] and Luisa M. Pastrana-Martínez *[ID]

Carbon Materials Research Group, Department of Inorganic Chemistry, Faculty of Sciences, University of Granada, Avda. Fuente Nueva, s/n ES18071 Granada, Spain; alpemo@correo.ugr.es (Á.P.-M.); semoto@ugr.es (S.M.-T.); fjmaldon@ugr.es (F.J.M.-H.)

* Correspondence: lpastrana@ugr.es; Tel.: +34-958240443

check for updates

Abstract: Functionalized graphene derivatives including graphene oxide (GO), reduced graphene oxide (rGO), and heteroatom (nitrogen/sulphur (N/S) or boron (B))-doped graphene were used to synthesize composites with TiO$_2$ (T). The photocatalytic performance of composites was assessed for the degradation of Orange G dye (OG) under simulated solar light. All the prepared graphene derivatives—TiO$_2$ composites showed better photocatalytic performance than bare TiO$_2$. A higher photocatalytic activity was found for the composites containing GO and N/S co-doped rGO (k_{app} = 109.2 × 10^{-3} and 48.4 × 10^{-3} min^{-1}, for GO-T and rGONS-T, respectively). The influence of both initial solution pH and the reactive species involved in the OG degradation pathway were studied. The photocatalytic activity of the samples decreased with the increase of the initial pH (from 3.0 to 10.0) due to the occurrence of electrostatic repulsive forces between the photocatalysts surface and the molecules of OG, both negatively charged. The use of selective scavengers showed that although the photogenerated holes dominate the degradation mechanism, radicals and singlet oxygen also participate in the OG degradation pathway. In addition, reutilization experiments indicated that the samples were stable under the reaction conditions used.

Keywords: graphene oxide; TiO$_2$; heteroatom doping; photocatalysis; Orange G; scavengers

1. Introduction

The growing industry and population is leading to a decrease of water resources quality. Up to date, several contaminants have been detected in water and wastewater such as nitrates, phosphates, metals, dyes, pesticides, pharmaceuticals, personal care products, endocrine disruptors, etc. Organic dyes are pollutants especially difficult to remove because of their high solubility and stability [1]. Advanced oxidation processes (AOPs) are considered efficient treatments for water polluted with recalcitrant and non-biodegradable compounds [2]. Heterogenous photocatalysis is a very attractive option because it is possible to use sunlight, the availability of non-poison materials, and low cost. In addition, it has demonstrated a high efficiency in degrading a wide range of water pollutants [3–5]. Among the various semiconductors used as photocatalysts such as TiO$_2$, ZnO, ZrO$_2$, CdS, ZnS, WO$_3$ etc., TiO$_2$ has been typically studied because of its high efficiency and stability for the degradation of inorganic and organic pollutants. However, its application in the visible range of the solar spectrum is limited by the low quantum yield and the wide band gap of TiO$_2$ (i.e., 3.2 eV for anatase) [6–9]. Several strategies have been developed to expand the response of TiO$_2$ into the visible range spectra namely, the addition of electron donors [10], noble metals [11], metal ion or anion doping [12,13], dye sensitization [14], synthesis of TiO$_2$ with exposed {001} facets [15], heterojunction with different types of active materials [16,17], combination with carbon materials [18], etc.

Carbon materials such as graphene (a two-dimensional allotrope of carbon) and its well-known derivatives including graphene oxide (GO) and reduced graphene oxide (rGO) have demonstrated the ability to enhance the photocatalytic performance of TiO_2 by producing a synergistic effect between both phases [18,19]. In fact, the delocalized conjugated system of π bonds in graphene materials could accept photogenerated electrons, avoiding the electron-hole recombination. Furthermore, the presence of oxygenated functionalities on GO (and in less extent in the case of rGO) could provide reactive sites to facilitate the assembly of the semiconductors and graphene sheets [19].

Different methods of synthesis have been used for the preparation of graphene based-TiO_2 composites for photocatalytic applications including the degradation of organic pollutants, production of H_2, reduction of CO_2, as well as supercapacitors, among others, under visible illumination. Liang et al. [20] reported the synthesis of rGO-TiO_2 composites by a one-step hydrothermal method and using ethanol/water as a reducing agent, with complete dye (Rhodamine B) degradation being achieved under UV–Vis irradiation for 30 min. Zhao et al. [21] used a two-step method (based on the hydrolysis and vacuum furnace at 700 °C) for the preparation of graphene-TiO_2 composites to remove 70% of methylene blue under visible light irradiation (λ = 450 nm) for 200 min. Other authors [22] reported Pt/GO-TiO_2 composites by the hydrothermal method with TiO_2 nanocrystals with exposed {001} and {101} facets for selective CO_2 conversion to CH_4, resulting in the selectivity of CO_2 conversion to the CH_4 product closely to 100% under simulated solar irradiation. Fattahi et al. [23] prepared graphene-TiO_2 composites by simultaneous hydrothermal synthesis and GO reduction. The photocatalytic performance of these composites for the formation of 2-hydroxyterephthalic acid (HTPA) under visible light (λ = 405 nm) was optimized by changing different synthesis parameters, such as stirring time and speed, the load of TiO_2 and GO, reaction time and ethanol/water ratio. They obtained an increase of the HTPA formation rate for the optimized graphene-TiO_2 composite in comparison with bare TiO_2. Police et al. [24] reported the synthesis of rGO-TiO_2 nanotube composites by the hydrothermal method showing a remarkable photocatalytic activity towards H_2 production (12.9 times higher than commercial TiO_2 under natural sunlight), as well as in other applications such as supercapacitors. Recently, Ashraf et al. [25] reported the synthesis of graphene/TiO_2/Ag composites by the combination of a sonochemical method and freeze-drying with a high visible light photocatalytic activity for the degradation of an azo dye (C.I. Reactive Yellow 2). They obtained 100% of dye degradation after 90 min under visible light.

Nevertheless, the optimization of the electronic properties of graphene is a critical topic today and growing interest has been devoted to the use of heteroatom-doped graphene (rather than the addition of noble metals) to produce high-performance photocatalytic composites under visible light. Chemical doping with heteroatoms such as oxygen (O) [26], nitrogen (N) [27–29], boron (B) [30], phosphorus (P) [31], or sulfur (S) [32,33], etc., can improve the photocatalytic performance of graphene materials by tailoring its electronic properties [34] and increasing their reactive catalytic sites to be used such as catalysts supports or even as a photocatalyst on their own [35].

Mou et al. [36] fabricated a composite based on N-doped rGO-TiO_2 through a solvothermal treatment showing higher photocatalytic activity for H_2 production in comparison with the composite prepared with rGO. Pedrosa et al. [37] synthetized N- and S-doped rGO-TiO_2 composites for the degradation of a pharmaceutical compound observing that the oxygen content in the precursor material plays an important role in the catalytic performance. Another study reported [38] the degradation of ca. 95% and 70% of methylene blue and 50% and 65% of rhodamine B in 60 min using B- or N-doped graphene-TiO_2 composites, respectively. The photocatalytic activity seems to be affected by the electronic structure of graphene.

However, the design of composites using graphene with an optimized concentration of external atoms and defects still remains a challenge in photocatalytic applications and needs to be more exhaustively studied [34,37,39,40].

In the present work, GO was co-doped with different heteroatoms, in particular N/S or B, following a hydrothermal process. Graphene derivatives were used to synthesize composites with TiO_2 by the

liquid phase deposition method. The synthetized materials were deeply characterized in order to identify the effect of different heteroatoms on their physicochemical properties and photocatalytic performance. The photodegradation of Acid Orange G (OG) dye under simulated solar radiation was studied as a reaction model for the catalysts screening. The selected azo dye is typically used in the paper and textile industry showing carcinogenic and mutagenic activity [41–44]. The optimization of experimental conditions (i.e., pH), the identification of photoactive species, as well as the stability of materials was also evaluated.

2. Materials and Methods

2.1. Synthesis of Graphene Oxide (GO)

GO was synthetized from graphite (powder < 20 μm) following the modified Hummers method [45]. Briefly, 240 mL of sulfuric acid, H_2SO_4 (96–99%, supplied by PanReac AppliChem, Darmstadt, Germany) was added slowly on both 5 g of graphite (Sigma-Aldrich, St. Louis, MO, USA) and 5 g of sodium nitrate, $NaNO_3$ (99%, Acros Organics, Geel, Belgium, keeping it under agitation and controlling the temperature with an ice bath. Then, 30 g of potassium permanganate, $KMnO_4$ (99%, PanReac AppliChem, Darmstadt, Germany) was added slowly under stirring to the above solution and heated at 35 °C for 10 h. Afterwards, 1000 mL of water and 30 mL of hydrogen peroxide, H_2O_2 (30% w/w, PanReac AppliChem, Darmstadt, Germany) were added very slowly to the suspension and after 30 min, the material was filtered. The obtained paste was washed repeatedly with water until it reaches pH of 5.5–6.0. The graphite oxide material obtained was dispersed in water (1.0 g in 500 mL) and sonicated for 1 h.

2.2. Synthesis of Heteroatom Reduced Graphene Oxide (rGO)

N/S- and B-doped graphene were prepared with a GO suspension (1.0 g L^{-1}) and thiourea, CH_4N_2S (99%, Alfa Aesar, Haverhill, MA, USA) [46], or boric acid, H_3BO_3 (Acros Organics, Geel, Belgium) [40], as N/S or B precursors, respectively by hydrothermal reduction [47]. The GO: Precursor ratio was selected as 1:10, in agreement with the optimized value in a previous study [46]. In a typical synthesis, an appropriate amount of thiourea or H_3BO_3 was dissolved into 60 mL of GO suspension and stirred for 10 min followed by sonication for 15 min. The above mixture was placed into a 100 mL Teflon vessel and sealed in a stainless-steel autoclave (Parr Instruments, Moline, IL, USA, Mod. 4748) to perform a hydrothermal treatment in an oven at 180 °C for 12 h. The resultant materials were washed with distilled water and exchanged with *tert*-butanol for 48 h. Finally, the freeze-drying process was used to remove the solvent (20 h). The materials were labelled as rGONS or rGOB when using thiourea or boric acid as precursors, respectively. The rGO material was also synthetized with comparative purposes, following the same procedure but without the addition of thiourea or boric acid.

2.3. Synthesis of Graphene Derivative-TiO2 Composites

The synthesis of the photocatalytic composites was carried out by the liquid phase deposition method (LPD), as previously reported [6]. Briefly, the precursors, ammonium hexafluorotitanate (IV), $(NH_4)_2TiF_6$ (99%, Sigma-Aldrich, St. Louis, MO, USA), and H_3BO_3 (0.1 and 0.3 mol L^{-1}, respectively) were added to a 100 mg L^{-1} suspension of GO, rGO, rGONS, or rGOB. The carbon loading was maintained at ~3.5 wt%. The mixture was heated in a silicon bath at 60 °C for 5 h under dynamic stirring. The precipitate was filtrated under a vacuum, washed repeatedly with distilled water, and dried at 80 °C for 8 h. Finally, the obtained solid was treated under N_2 flow in an oven at 200 °C, 5 °C min^{-1} for 2 h. Bare TiO_2 (referred as TiO_2) was also synthetized following the same methodology, without the addition of any graphene derivative. The TiO_2 composites prepared with GO, rGO, rGONS, and rGOB are denoted, as GO-T, rGO-T, rGONS-T, and rGOB-T, respectively.

2.4. Characterization Techniques

A thermogravimetric (TG) analysis of the composites was determined by heating from 40 to 950 °C (air flow) at 20 °C min^{-1} using a SHIMADZU TGA-50H thermobalance. The NICOLET 510P spectrometer with an attenuated total reflection accessory and a ZeSn as ATR crystal was used for the determination of ATR-IR spectra. An elemental CHNS-O Analyzer Flask (1112 Series) from Thermo Finigan was used to obtain the total oxygen content of samples. The N$_2$ adsorption-desorption isotherms at −196 °C were carried out using a Quantachrome Quadrasorb SI equipment. The Brunauer–Emmett–Teller (BET) equation was applied to calculate the apparent surface area (S$_{BET}$) [48,49]. Pore size distributions and the mean pore diameter (d$_{pore}$) were determined by using the quenched solid density functional theory (QSDFT) as reported elsewhere [19]. The total pore volume (V$_{total}$) was obtained considering the volume of N$_2$ adsorbed at P/P$_0$ = 0.95 [50]. The point zero of charge (pH$_{PZC}$) of the materials was determined following the method described elsewhere [51,52]. The LEO (Carl Zeiss) GEMINI-1430-VP microscope was used to analyze the morphology of the materials by scanning electron microscopy (SEM). The X-ray diffractograms were obtained in a Philips PW 1710, using the CuKα radiation and a nickel filter that removes the κβ radiation. The average crystal size of the samples was determined using the Scherrer equation. The UV–Vis spectrophotometer (CARY 5E from VARIAN) equipped with a diffuse reflectance accessory (DRA) was used for the analysis of the optical properties of photocatalysts. The band gap of the materials was calculated from the corresponding Tauc plots using (Abs·hν)$^{1/2}$ units as a function of energy (eV).

2.5. Photocatalytic Experiments

The photocatalytic degradation of Acid Orange G (OG) dye (Sigma-Aldrich, St. Louis, MO, USA) was evaluated under simulated solar light at ca. 28 °C. In a typical experiment, a Pyrex reactor was filled with 50 mL of OG aqueous solution (20 mg L^{-1} or 4.42 × 10^{-5} mol L^{-1}). During the photocatalytic experiment, the aqueous solution was stirred with a magnet and an oxygen flow was used. The concentration of the photocatalyst was 1.0 g L^{-1}.

The experiments were performed with a 500 W m^{-2} of irradiance power using a SOLAR BOX 1500 e (CO.FE.MEGRA, Milano, Italy) with a 1500 W Xenon lamp. In order to establish the adsorption-desorption equilibrium, the suspensions were maintained in absence of light during 60 min. Samples were withdrawn from the reaction mixture and filtered with polyether sulfone syringe filters (0.45 μm pore size). Photolysis experiments (in the absence of catalyst) were also performed. Samples were analyzed using a UV-spectrophotometer model UV-1800 Shimadzu. For all the photocatalytic experiments, the absorption spectra (λ$_{máx}$ = 485 nm) of OG were measured at different reaction times. The total organic carbon (TOC) analysis was performed in a Shimadzu TOC-5000A apparatus. The experiments were performed at different pH values, i.e., 3.0, 6.0 (natural), and 10.0, by adding HCl 0.1 or NaOH 0.1 M, respectively. The photocatalytic degradation pathway of OG was studied using an ethylenediaminetetraacetic acid (EDTA, 1.0 mM), furfuryl alcohol (FFA, 1.0 mM), *tert*-butanol (*t*-BuOH, 1.0 mM), and as a hole, singlet oxygen ($^1O_2$) and radical scavengers, respectively [6].

The photocatalytic degradation can be described by the following equation:

$$[OG] = [OG]_0 \times e^{-k_{app} \times t} \tag{1}$$

where k_{app} is the pseudo-first order kinetic constant, t is the reaction time, and [OG]$_0$ and [OG] denote the pollutant concentration at t = 0 and t = t, respectively. The values of k_{app} were obtained by a non-linear regression.

3. Results and Discussion

3.1. Materials Characterization

The graphene content (wt%) in all the prepared composites was analyzed by TG (not shown) calculated from the weight loss of the respective graphene derivative-TiO_2 composites by burning the carbon phase during the TG experiments under air flow. The results corroborated at ca. 4.0 wt% carbon (in agreement with the nominal carbon content, i.e., ~3.5%). This content was chosen in accordance with the best photocatalytic activity of the composites prepared with TiO_2 and GO, as reported elsewhere [6,19].

The ATR-IR spectra of bare TiO_2, GO, and doped graphene samples are displayed in Figure 1. The TiO_2 spectrum shows a band at ca. 850 cm^{-1} associated to the Ti-O vibration [53]. The presence of a band at around 1640 cm^{-1} is related to the presence of the Ti-OH group as well as the bending vibration of coordinated water [50,53], while the TiO_2 lattice vibrations are assigned to the peak at ca. 1420 cm^{-1} [54,55].
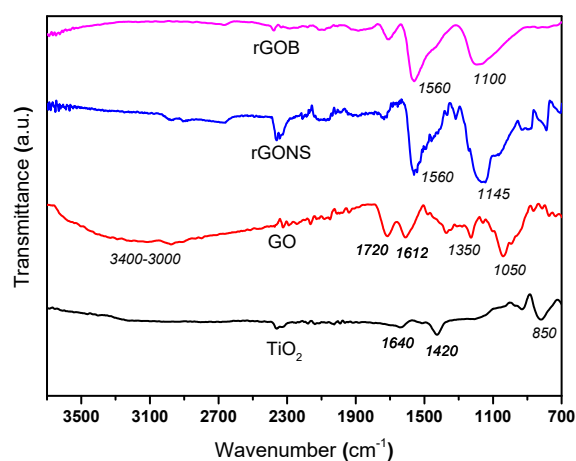

Figure 1. FT-IR spectra of TiO_2 (T), graphene oxide (GO), reduced graphene oxide nitrogen/sulphur (rGONS), and reduced graphene oxide boron (rGOB).

For the GO spectrum, different bands were observed related to the presence of oxygen functionalities. The bands at ca. 1050 and 1350 cm^{-1} are assigned to the stretching vibration of C-O and to the stretching of C-OH groups, respectively while the bands at ca. 1612, 1720, and around 3000–3400 cm^{-1} are attributed to the skeletal vibration of graphene sheets, to carbonyl groups (C=O), and to the vibrations of C-OH groups, respectively [19].

Regarding the rGONS sample, the FT-IR spectrum shows two main peaks, one of them associated to the vibration of sp^2 aromatic C=C and C=N bonds at ca. 1560 cm^{-1} and another attributed to the stretching vibration of the C-S-C groups at ca. 1100–1145 cm^{-1} [37,46,56–58]. In the case of rGOB, there are also two main peaks in the spectrum, attributed to the vibration of C=C bond (at ca. 1560 cm^{-1}) and to the vibration of B-C bond and C-O bond (at ca. 1100 cm^{-1}), as previously observed [46,59]. On the other hand, the peaks associated to the oxygen functional groups in the doped-graphene materials exhibited lower intensities in comparison with the obtained for the GO sample (Figure 1). These results could be due to the partial removal of these groups after hydrothermal treatment. Thus, the elemental analysis of the graphene-based materials indicated a percentage of oxygen content (wt%) of 53.5%, 23.2%, and 21.4%, for GO, rGO, and rGONS, respectively (results not shown). These results suggested a considerable deoxygenation as well as heteroatom incorporation (ca. 1.8% and 1.3%, for N and S, respectively).

The XPS analysis of the rGONS sample (labelled as rGO-NS-10) and B-doped graphene (prepared by a similar synthesis procedure to the rGOB sample) was obtained and discussed in previous studies [40,46]. The nitrogen species in the rGONS material were the amino group (-NH_2),

N-pyridinic species (N6), N-pyrrolic form (N5), and N-graphitic (NQ), whereas the sulphur groups correspond mainly to S-thiophene. Regarding the rGOB sample, the most intense peak corresponds to boron replacing carbon in the hexagonal lattice (i.e., BC_3).

Physical adsorption of N_2 at -196 °C was carried out to determine the textural properties of the materials. Table 1 summarizes the apparent surface area (S_{BET}), total pore volume (V_{pore}), and the mean pore diameter (d_{pore}) of the materials. N_2 adsorption-desorption isotherms for TiO_2 and the prepared graphene derivative—TiO_2 composites are shown in Figure 2a. The N_2 isotherms of the samples showed an adsorptive behaviour of type-IV (in agreement with the IUPAC classification) [48], attributed to mesoporous materials. The larger volume of adsorbed N_2 at high relative pressures can be related to capillary condensation in mesopores. Moreover, the presence of a hysteresis loop of type H3 in the samples could be due to the adsorbents with slit-shaped pores or the presence of aggregates formed by plate particles as reported elsewhere [6,50].

Table 1. Brunauer–Emmett–Teller (BET) surface area (S_{BET}), total pore volume (V_{pore}), mean pore diameter (d_{pore}), pH at the point of zero charge (pH_{PZC}), band-gap energy (E_g), and crystallite size of synthetized materials.

Samples	S_{BET} (m^2 g^{-1})	V_{pore} (cm^3 g^{-1})	d_{pore} (nm)	pH_{PZC}	E_g (eV)	Crystallite Size (nm)
TiO_2	43	0.12	5.2, 10.3	3.5	3.20	9.7 ± 1.3
GO-T	55	0.17	4.2, 16.7, 25.2	3.1	2.98	12.1 ± 1.2
rGO-T	50	0.13	5.2, 10.3	3.2	3.15	–
rGONS-T	40	0.08	5.0, 7.1	3.3	3.12	7.6 ± 1.3
rGOB-T	80	0.20	5.0	3.2	3.12	8.9 ± 1.2

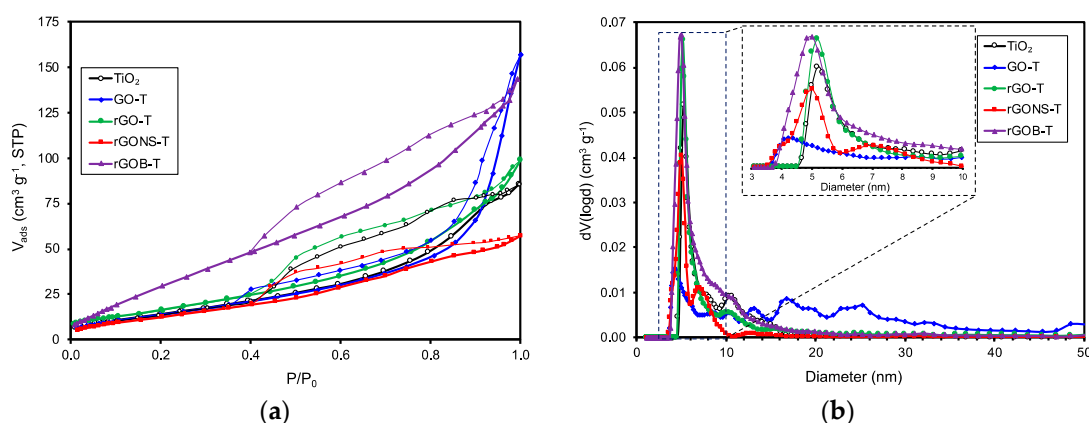**Figure 2.** (**a**) N_2 adsorption-desorption isotherms and (**b**) pore size distributions obtained by the quenched solid density functional theory (QSDFT) method of TiO_2, GO-T, rGO-T, rGONS-T, and rGOB-T.

In general, TiO_2 and graphene based-TiO_2 composites exhibited surface areas, S_{BET}, of ca. 40–80 m^2 g^{-1}, rGOB-T being the sample with the highest surface area (80 m^2 g^{-1}). In general, all the prepared composites with graphene derivatives presented a higher total pore volume than the TiO_2 sample. The pore size distribution (PSD) of the samples are depicted in Figure 2b. The results indicated mean pore sizes between 5.0 and 10.3 nm, with the exception of GO-T that presented a wider PSD with larger mesopores, i.e., 16.7 and 25.2 nm. This fact could be associated to the high amount of oxygen functionalities, which facilitate the separation of graphene layers and coating of TiO_2 particles during the synthesis of composite preparation.

The pH_{pzc} values obtained for both TiO_2 and composite materials presented an acidic character, i.e., $pH_{pzc} = 3.0$–3.5 (Table 1), which should be explained with TiO_2 precursors, the low temperature treatment (200 °C), and the presence of acidic groups on graphene surfaces.

Figure 3 shows representative SEM micrographs of TiO_2 and graphene-based composites. The morphology of TiO_2 (Figure 3a) shows spherical particles aggregated with each other forming a cluster of TiO_2 particles.
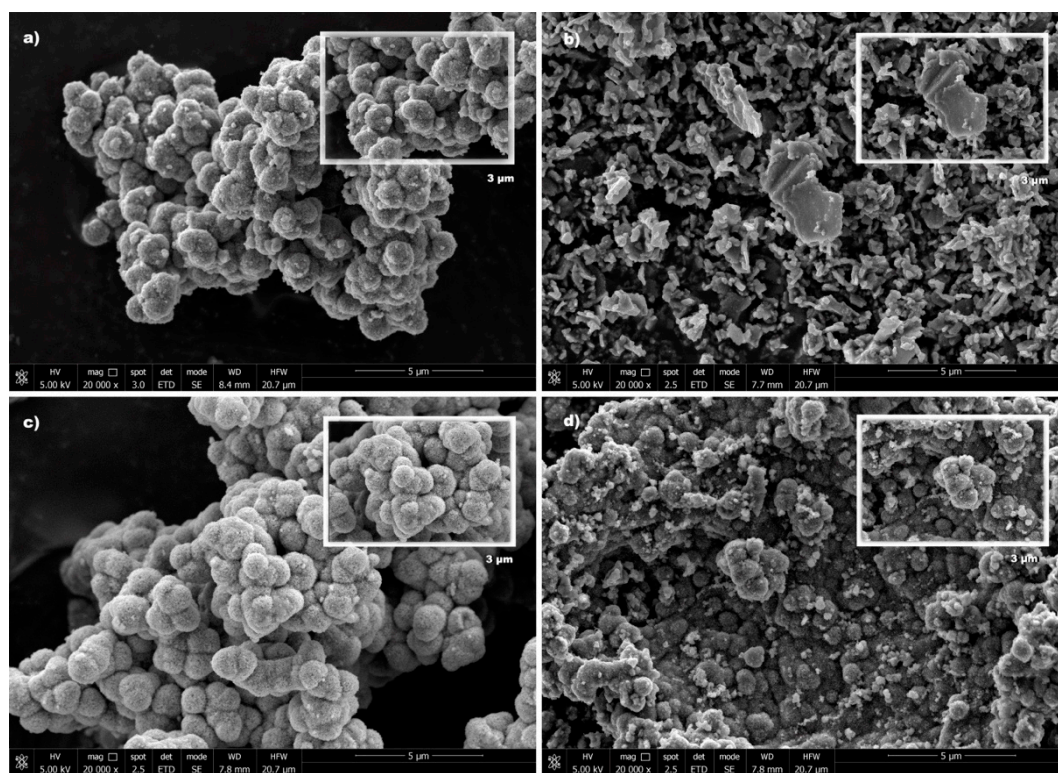

Figure 3. SEM micrographs of (**a**) TiO_2, (**b**) GO-T, (**c**) rGONS-T, and (**d**) rGOB-T.

The SEM micrograph of the GO-T composite (Figure 3b) shows a well distribution of TiO_2 particles around the GO sheets resulting in the formation of a kind of platelets uniformly covered by TiO_2 nanoparticles [6]. Different morphologies were obtained for the heteroatom doped-graphene-TiO_2 composites (Figure 3c,d) in comparison with the morphology observed for GO-T, since the presence of well-separated platelets was not so notorious. The surface morphology of rGONS-T and rGOB-T seems to be similar to that of bare TiO_2 presenting larger or smaller clusters of particles, respectively.

The XRD patterns of the TiO_2, GO-T, rGONS-T, and rGOB-T samples are depicted in Figure 4a. TiO_2 anatase particles were detected in all the prepared materials. The major diffraction peaks at 2θ values of 25.2, 37.7, 48.1, and 53.5° were associated to the lattice planes of (101), (004), (200), and (105), respectively [60]. No significant diffraction peaks of carbon were observed in the XRD patterns of GO-T, rGONS-T, and rGOB-T composites. These results could be associated to the low amount of carbon material present in the composites (i.e., 3%–4%). Particles sizes of 9.7, 12.1, 7.6, and 8.9 nm were calculated for TiO_2, GO-T, rGONS-T, and rGOB-T photocatalysts, respectively (Table 1) displaying the doped-graphene composites with N/S or B, lower particles sizes in comparison with both GO-T and TiO_2.

The UV–Vis absorption spectra of TiO_2 and graphene derivative-TiO_2 composites are depicted in Figure 4b. For all the samples, a strong band at ca. <400 nm corresponding to the intrinsic bandgap transition of TiO_2 was observed. Furthermore, all the graphene-TiO_2 composites (i.e., GO-T, rGONS-T, and rGOB-T) display a decrease in wavelength on the TiO_2 absorption band. These results can be associated to the electronic interaction between semiconductor and carbon as well as to the occurrence of defect in the structure of TiO_2 [61]. Moreover, it is noteworthy that for all the graphene-TiO_2 materials an increase of the absorption range at a wavelength higher than 380 nm (visible range) in comparison with TiO_2 was observed. This effect is normally associated to the intrinsic light absorption

capacity of graphene as a carbon material and also to the electronic transitions between both phases [37]. The inset of Figure 4b exhibits the Tauc's plots versus the energy (eV). The calculated E_g of TiO_2, GO-T, rGONS-T, and rGOB-T were 3.20, 2.98, 3.12, and 3.12 eV, respectively (Table 1). The lowest E_g of GO-T and the graphene-doped composites in comparison with bare TiO_2 may be associated to the presence of Ti-O-C bonds between carbon materials and TiO_2 [37].
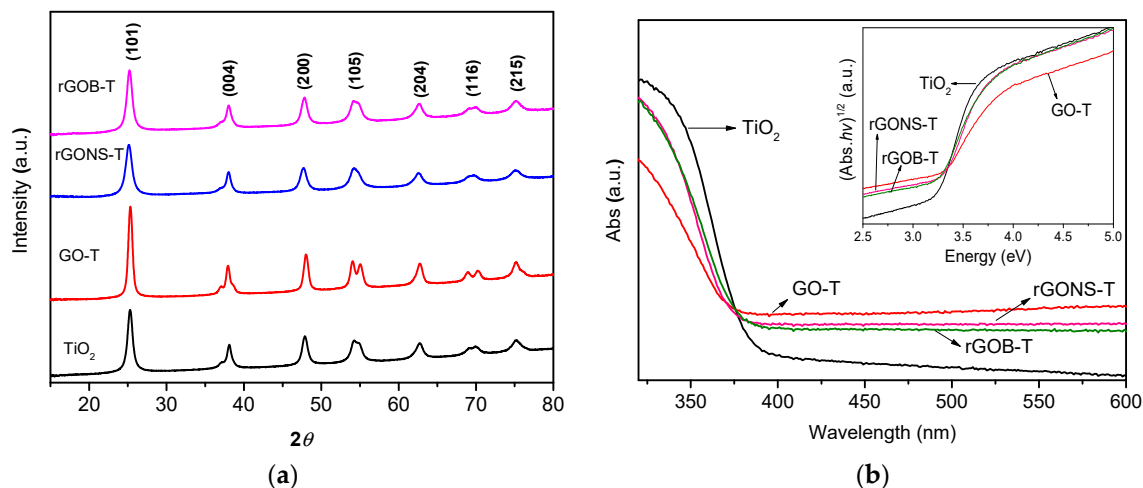

Figure 4. (**a**) XRD patterns of TiO_2, GO-T, rGONS-T, and rGOB-T, (**b**) UV–Vis spectra and Tauc's plots versus the energy in eV of TiO_2 and graphene derivative-TiO_2 composites (inset).

3.2. Photocatalytic Degradation of OG

The photocatalytic performance of TiO_2 and graphene derivatives-TiO_2 composites for OG degradation (at natural pH, 6.0) under simulated solar light is shown in Figure 5. The OG conversion after 60 min (X_{OG}), pseudo-first order kinetic rate constant (k_{app}), and regression coefficient (r^2) are summarized in Table 2. The photolysis experiment was carried out in the absence of a photocatalyst and under simulated solar light. Under these conditions, the degradation of OG was approximately 6.0% after 60 min, indicating that the pollutant is very light-stable under non-catalytic conditions. On the other hand, dark phase experiments (in the absence of light) were also performed to evaluate the adsorption capacity of the materials (not shown). The results obtained were 6.0%, 10.0%, 8.0%, 8.0%, and 7.0% for TiO_2, GO-T, rGO-T, rGONS-T, and rGOB-T, respectively, detecting that the adsorption equilibrium was reached after 60 min for all the photocatalysts. Once the adsorption-desorption equilibrium was achieved, OG degradation experiments were carried out under simulated solar light.
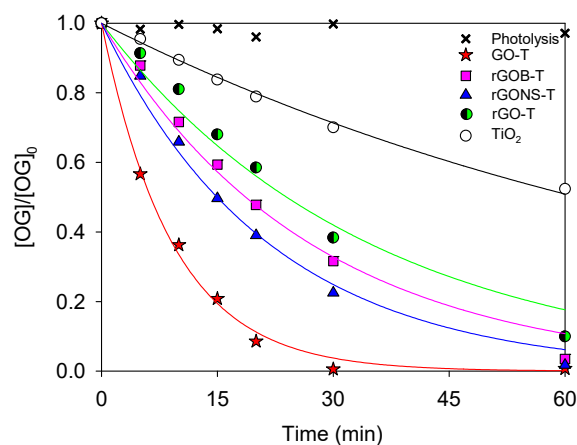

Figure 5. Normalized concentration of OG (Orange G dye) as a function of time in photolysis and photocatalysis (TiO_2, rGO-T, GO-T, rGONS-T, and rGOB-T).

Table 2. OG conversion after 60 min (X_{OG}), pseudo-first order kinetic rate constant (k_{app}), and regression coefficient (r^2) of OG.

Sample	*pH*	X_{OG} (%)	k_{app} (10^{-3} min^{-1})	r^2
Photolysis	6.0	2.8	––	––
TiO$_2$	6.0	47.6	11.2 ± 0.3	0.996
GO-T	6.0	99.8	109.2 ± 4	0.996
rGO-T	6.0	90.0	29.0 ± 3	0.97
rGONS-T	6.0	98.2	48.4 ± 2	0.993
rGOB-T	6.0	96.5	39.1 ± 2	0.99
GO-T	**3.0**	100.0	153.4 ± 8	0.992
GO-T	**10.0**	99.6	55.1 ± 3	0.98
GO-T + EDTA	6.0	22.1	4.5 ± 0.4	0.95
GO-T + *t*-BuOH	6.0	75.4	24.1 ± 1	0.996
GO-T + FFA	6.0	66.3	16.6 ± 1	0.98
rGONS-T	**3.0**	99.5	62.0 ± 3	0.992
rGONS-T	**10.0**	87.1	39.1 ± 1	0.994
rGONS-T + EDTA	6.0	16.4	3.4 ± 0.3	0.91
rGONS-T + *t*-BuOH	6.0	71.1	21.3 ± 0.3	0.999
rGONS-T + FFA	6.0	46.9	12.1 ± 0.8	0.95

The presence of graphene derivatives, such as GO, rGO, rGONS, and rGOB, increased the efficiency for the OG degradation in comparison with TiO$_2$ (OG conversion of 99.8%, 90.0%, 98.2%, 96.5%, and 47.6% for GO-T, rGO-T, rGONS-T, rGOB-T, and TiO$_2$ respectively, Figure 5 and Table 2). These results suggest a synergistic effect between graphene materials and TiO$_2$, although this effect depends on the type of graphene derivative used in the composite. In particular, the composite prepared with GO (i.e., GO-T) showed the best performance for the OG degradation under simulated solar light (k_{app} = 109.2 × 10^{-3}). The results of TOC removal were found to follow the same trend as a photocatalytic conversion, i.e., GO-T, rGONS-T, rGOB-T, rGO, and TiO$_2$ produced respectively 40%, 22%, 17%, 17%, and 15% of TOC reduction after 60 min of solar irradiation.

The lower photocatalytic activity obtained for rGO-T, rGONS-T, and rGOB-T when compared with the GO-T composite could be attributed to the lower amount of oxygen functionalities, resulting in a weaker interaction between graphene derivatives and TiO$_2$. The lowest band gap energy of the GO-T composite (Table 1) as well as the pronounced quenching of photoluminescence in the GO-T composite [6], suggest that GO can effectively accept the photoexcited electrons to hinder electron-hole recombination. These effects combined with the good assembly and interfacial coupling between the TiO$_2$ and the GO sheets, as observed by SEM images (Figure 3b), may promote charge migration between both phases after photoexcitation, leading to an increase in the efficiency of the photocatalytic process for the GO-T composite.

Nevertheless, the doped graphene derivative-TiO$_2$ composites also showed better performance when compared with both rGO-T and bare TiO$_2$. These results can be explained due to the presence of N/S or B-doping, which favoured a lower band-gap energy (E_g) for both rGONS-T and rGOB-T in comparison with rGO-T and TiO$_2$ materials (3.12, 3.12, 3.15, and 3.20 eV, respectively, Table 1). The photocatalytic activity can be also related with the enhancement of electronic conductivity as well as the recovery of the sp^2 graphene network and the decrease of defects within the plane associated with heteroatom incorporation [34,36,62]. In general, the results suggest that the addition of any graphene derivative in the TiO$_2$ matrix can promote the photocatalytic activity of TiO$_2$ under solar light due to the charge transfer of photo-generated electrons between TiO$_2$ and graphene that can limit the electron-hole recombination, permitting the graphene-TiO$_2$ composites to produce a higher amount of radicals under solar radiation [63]. Both GO-T and rGONS-T materials were selected to

study the effect of initial pH on the OG conversion, the photoactive species involved in the reaction, and reusability cycles.

3.2.1. Influence of pH on OG Degradation

The photocatalytic degradation of OG at initial pH values of 3.0, 6.0 (natural pH), and 10.0 is shown in Figure S1a,b of the Supplementary Materials for both GO-T and rGONS-T, respectively. The obtained k_{app} constants for the different pH values are illustrated in Figure 6 while the OG conversion (X_{OG}), rate constant (k_{app}), and regression coefficient (r^2) at different pH values are summarized in Table 2.
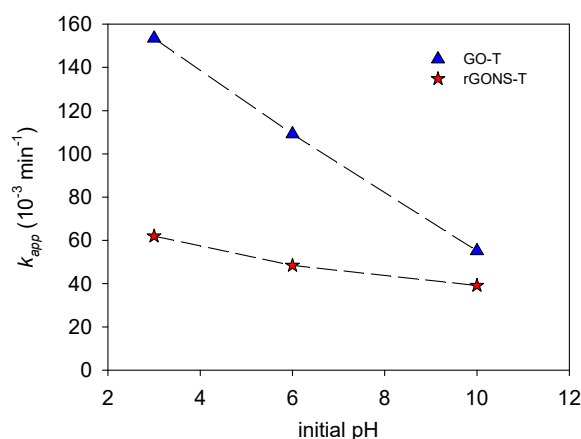
Figure 6. Pseudo-first order kinetic rate constant (k_{app}) for different initial solution pH over the GO-T and rGONS-T composites.

It can be observed that the photocatalytic performance of photocatalysts decreased as the initial pH value increased, as observed for the reaction rate constants for both materials when the initial pH increased from pH 3.0 to 10.0 (k_{app} = 153.4 × 10^{-3} and 62.0 × 10^{-3} min^{-1} for GO-T and rGONS-T, respectively for pH 3.0 and k_{app} = 55.1 × 10^{-3} and 39.1 × 10^{-3} min^{-1} for GO-T and rGONS-T, respectively for pH 10.0, Figure 6).

It is well known that the initial pH value can modify the surface charge density of catalyst and the ionization state of organic molecules at the same time, among others [64]. For pH values higher than the pH_{PZC} of TiO_2, the surface charge becomes negative (TiO^-), while for pH values lower than the pH_{PZC}, the surface charge is positive ($TiOH_2^+$). OG is a molecule with a negative charge (OG^-) in the solution due to the deprotonation of the sulfonic group $^-SO_3$, (pK_a = 1.0) [65]. When the initial pH is 3.0, the surface of both GO-T ($pH_{PZC} \approx 3.1$) and rGONS-T ($pH_{PZC} \approx 3.3$) is positively charged, while OG is negatively charged. Thus, electrostatic attraction forces are expected. On the contrary, at higher pH values (i.e., natural pH of 6.0 and 10.0), a lower photodegradation rate for both materials was observed due to the occurrence of electrostatic repulsive forces between the negatively charged catalysts surface and the OG^- species.

3.2.2. Photocatalytic Degradation Pathway

The photoactive species involved in the reaction were investigated at natural pH (6.0) using EDTA, FFA, and t-BuOH, as scavengers for holes, singlet oxygen ($^1O_2$), and radicals, respectively. Figure 7a,b displays the OG concentration during the photocatalytic experiments with the addition of the scavengers for the GO-T and rGONS-T composites, respectively. The results indicate that for both photocatalysts the presence of any scavenger produces a decrease in the OG degradation rate, suggesting that photogenerated holes, $^1O_2$, and radical species participate in the OG degradation pathway.
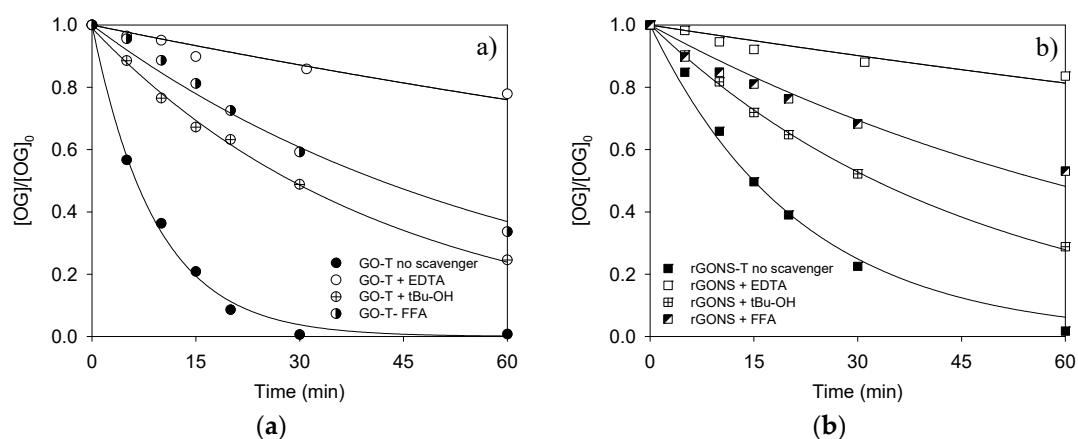
Figure 7. Normalized concentration of OG as a function of time with and without scavengers for (**a**) GO-T and (**b**) rGONS-T.

For GO-T (Figure 7a), the addition of FFA and t-BuOH reduced the k_{app} from 109.2×10^{-3} to 24.1×10^{-3} min^{-1} and from 109.2×10^{-3} to 16.6×10^{-3} min^{-1}, respectively. Nevertheless, the highest reduction of the constant rate was found in the presence of EDTA ($k_{app} = 4.5 \times 10^{-3}$ min^{-1}). Regardless, the rGONS-T material, an analogous performance was observed (Figure 7b) and although the presence of t-BuOH and FFA led to a reduction of the photocatalytic activity, the addition of EDTA produced the highest decrease in the rate constant (from 48.4×10^{-3} to 21.3×10^{-3}, 12.1×10^{-3} and 3.4×10^{-3} min^{-1}, respectively). These results suggest that the photoactive species including hydroxyl, superoxide anion, hydroperoxyl radicals, and singlet oxygen (i.e., HO$^{\bullet}$, O$_2^{\bullet-}$, HOO, and ^{1}O$_2$, respectively) participate in the photodegradation mechanism [66,67]. However, the high quenching effect of EDTA indicates that photogenerated holes (h$^+$) play an essential role in OG removal for both GO-T and rGONS-T photocatalysts under simulated solar light.

3.2.3. Reutilization Tests

The photocatalytic stability of both GO-T and rGONS-T materials was examined. Four consecutive reusability cycles were performed at pH natural (pH = 6.0) under simulated solar light (Figure 8). The experiments were carried out as follows. After each run, the photocatalyst was filtered, washed with distilled water, and dried at 80 °C for 6 h. The resulting material was reused in the photocatalytic experiments using a fresh OG solution. The OG conversion decreased between the first and the second run for both photocatalysts (from 100% to 80.3% and from 98.2% to 70.1% for GO-T and rGONS-T, respectively), due to the adsorption of by-products on the photocatalyst. In the third run, the photocatalytic activity of the materials is essentially kept with a slight decrease of the OG conversion (i.e., from 80.3% to 75.0% and from 70.1% to 63.5% for GO-T and rGONS-T, respectively) and in the fourth run the photocatalytic performance of photocatalysts remained almost unchanged with respect to the third run concluding that both materials were stable under the reaction conditions used. Nevertheless, more studies will be required namely, the use in continuous flow reactors for the sake of checking the long-term stability of catalysts.
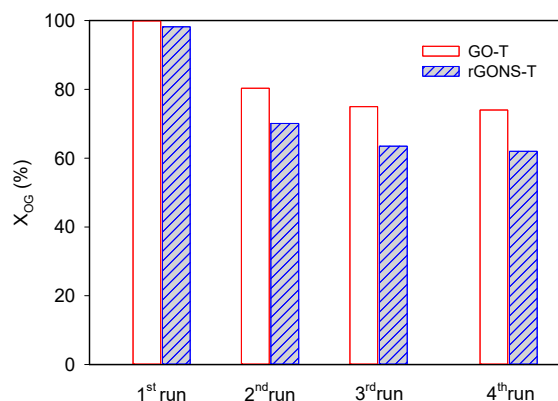
Figure 8. Reusability of the GO-T and rGONS-T photocatalysts for the OG degradation during four consecutive runs.

For comparison purposes, Table 3 comprises studies regarding graphene-TiO$_2$ based photocatalysts that have been recently published towards dye degradation under visible light illumination. It can be concluded that the obtained photocatalyst in this work showed a good photocatalytic performance comparatively to that of other materials reported in the literature.

Table 3. Compilation of recently published works regarding graphene-TiO$_2$ based photocatalysts for dye degradation under visible light illumination.

Photocatalyst	Application	Main Results	Ref.
N-TiO$_2$/rGO aerogel	20 mg L^{-1}, 100 mL MB	Excellent adsorption Removal rates > 90% in 60 min	[68]
N-TiO$_2$/rGO	10 mg L^{-1}, 50 mL RhB	Degradation of 90% in 120 min	[69]
GO/TiO$_2$/Hermin	10 mg L^{-1}, 250 mL RhB under UV/Vis/H$_2$O$_2$.	Degradation of 100% in 40 min	[70]
rGO/TiO$_2$/WO$_3$	MB	Degradation of 83% in 60 min	[71]
rGO/TiO$_2$	5 mg L^{-1}, 35 mL MB	Degradation of 82% in 140 min Conversion (TOC) 49% in 100 min	[72]
rGO/amino-grafted TiO$_2$	5 mg L^{-1}, MB 5 mg L^{-1}, Rh6G	Degradation of 91.2% in 40 min (MB) Degradation of 88.3% in 240 min (Rh6G)	[73]
Graphene aerogel/TiO$_2$/g-C$_3$N$_4$	20 mg L^{-1}, 25 mL RhB	Adsorption of 96.5% in 60 min Degradation of 98.4% in 60 min	[74]
GO-TiO$_2$	20 mg L^{-1}, 50 mL OG	Degradation of 99.8% in 60 min Conversion (TOC) 40% in 60 min	This work
rGONS-TiO$_2$	20 mg L^{-1}, 50 mL OG	Degradation of 98.2% in 60 min Conversion (TOC) 22% in 60 min	This work
rGOB-TiO$_2$	20 mg L^{-1}, 50 mL OG	Degradation of 96.5% in 60 min Conversion (TOC) 17% in 60 min	This work

MB: Mthylene blue; RhB: Rhodamine B; Rh6G: Rhodamine 6G; OG: Acid Orange G.

4. Conclusions

The morphology of the graphene-TiO$_2$ composite depends on the type of graphene derivative used during the synthesis. Thus, N/S- or B-doped graphene composites (rGONS-T and rGO-B) and undoped rGO composite (i.e., rGO-T) show clusters of TiO$_2$ particles, while the composite including GO (GO-T) presents a structure formed by graphene layers coated by TiO$_2$ particles. All materials were mesoporous and presented an acidic character. The addition of any graphene derivative triggers the narrowing band-gap energy in comparison with bare TiO$_2$.

The OG conversion and mineralization were always higher with the graphene derivative-TiO$_2$ composites rather than TiO$_2$ under simulated solar light.

The most active material consisted of GO in a TiO$_2$ matrix (GO-T). The photocatalytic performance is being related with the morphology of GO-T composite that shows a strong interaction between

graphene sheets and TiO_2 particles, producing an optimal assembly of TiO_2 on GO sheets as well as to the lowest band gap energy.

The photocatalytic performance of functionalized graphene derivatives-TiO_2 composites decreases as the initial solution pH increases, attaining a OG conversion of 100% and 99.5% for GO-T and rGONS-T, respectively at pH 3.0 due mainly to the occurrence of electrostatic attraction forces between the catalyst surface and OG molecules.

The addition of scavengers suggests that for both GO-T and rGONS-T catalysts, radical species, photogenerated holes, and singlet oxygen species participate in the OG degradation pathway. However, the higher reduction of the photocatalytic performance observed when EDTA is used as hole scavengers, indicates that photo-generated holes dominated the OG degradation on graphene-TiO_2 composites rather than radicals or singlet oxygen species. In addition, the reutilization cycles prove that both GO-T and rGONS-T composites were stable in a series of consecutive runs.

References

1. Brillas, E.; Martínez-Huitle, C.A. Decontamination of wastewaters containing synthetic organic dyes by electrochemical methods. An updated review. *Appl. Catal. B Environ.* **2015**, *166*, 603–643. [CrossRef]

2. Andreozzi, R.; Caprio, V.; Insola, A.; Marotta, R. Advanced oxidation processes (AOP) for water purification and recovery. *Catal. Today* **1999**, *53*, 51–59. [CrossRef]

3. Rodríguez, S.M.; Galvez, J.B.; Gasca, C.A.E. Photocatalysis. *Sol. Energy* **2004**, *77*, 443–444. [CrossRef]

4. Fujishima, A.; Honda, K. Electrochemical Photolysis of Water at a Semiconductor Electrode. *Nature* **1972**, *238*, 37–38. [CrossRef]

5. Inoue, T.; Fujishima, A.; Konishi, S.; Honda, K. Photoelectrocatalytic reduction of carbon dioxide in aqueous suspensions of semiconductor powders. *Nature* **1979**, *277*, 637–638. [CrossRef]

6. Pastrana-Martínez, L.M.; Morales-Torres, S.; Likodimos, V.; Figueiredo, J.L.; Faria, J.L.; Falaras, P.; Silva, A.M. Advanced nanostructured photocatalysts based on reduced graphene oxide–TiO_2 composites for degradation of diphenhydramine pharmaceutical and methyl orange dye. *Appl. Catal. B Environ.* **2012**, *123*, 241–256. [CrossRef]

7. Fujishima, A.; Rao, T.N.; Tryk, D.A. Titanium dioxide photocatalysis. *J. Photochem. Photobiol. C Photochem. Rev.* **2000**, *1*, 1–21. [CrossRef]

8. Konstantinou, I.; A Albanis, T. TiO_2-Assisted photocatalytic degradation of azo dyes in aqueous solution: Kinetic and mechanistic investigations. *Appl. Catal. B Environ.* **2004**, *49*, 1–14. [CrossRef]

9. Nakata, K.; Fujishima, A. TiO_2 photocatalysis: Design and applications. *J. Photochem. Photobiol. C Photochem. Rev.* **2012**, *13*, 169–189. [CrossRef]

10. Maeda, K.; Higashi, M.; Lu, D.; Abe, R.; Domen, K. Efficient Nonsacrificial Water Splitting through Two-Step Photoexcitation by Visible Light using a Modified Oxynitride as a Hydrogen Evolution Photocatalyst. *J. Am. Chem. Soc.* **2010**, *132*, 5858–5868. [CrossRef]

11. Yu, J.; Qi, L.; Jaroniec, M. Hydrogen Production by Photocatalytic Water Splitting over Pt/TiO_2Nanosheets with Exposed (001) Facets. *J. Phys. Chem. C* **2010**, *114*, 13118–13125. [CrossRef]

12. Liu, G.; Niu, P.; Sun, C.; Smith, S.C.; Chen, Z.-G.; Lu, G.M.; Cheng, H.-M. Unique Electronic Structure Induced High Photoreactivity of Sulfur-Doped Graphitic C$_3$N$_4$. *J. Am. Chem. Soc.* **2010**, *132*, 11642–11648. [CrossRef] [PubMed]

13. Weber, A.S.; Grady, A.M.; Koodali, R.T. Lanthanide modified semiconductor photocatalysts. *Catal. Sci. Technol.* **2012**, *2*, 683. [CrossRef]

14. Kim, W.; Tachikawa, T.; Majima, T.; Choi, W. Photocatalysis of Dye-Sensitized TiO$_2$ Nanoparticles with Thin Overcoat of Al$_2$O$_3$: Enhanced Activity for H2 Production and Dechlorination of CCl$_4$. *J. Phys. Chem. C* **2009**, *113*, 10603–10609. [CrossRef]

15. Police, A.K.R.; Vattikuti, S.P.; Baik, Y.-J.; Byon, C.; Vatikuti, S.P. Eco-Friendly, hydrogen fluoride-Free, morphology-Oriented synthesis of TiO$_2$ with exposed (001) facets. *Ceram. Int.* **2019**, *45*, 2178–2184. [CrossRef]

16. Police, A.K.R.; Vattikuti, S.V.P.; Mandari, K.K.; Chennaiahgari, M.; Mangalampalli, V.P.S.; Valluri, K.; Byon, C. Bismuth oxide cocatalyst and copper oxide sensitizer in Cu$_2$O/TiO$_2$/Bi$_2$O$_3$ ternary photocatalyst for efficient hydrogen production under solar light irradiation. *Ceram. Int.* **2018**, *44*, 11783–11791. [CrossRef]

17. Vattikuti, S.P.; Reddy, P.A.K.; Nagajyothi, P.; Shim, J.; Byon, C. Hydrothermally synthesized Na$_2$Ti$_3$O$_7$ nanotube–V$_2$O$_5$ heterostructures with improved visible photocatalytic degradation and hydrogen evolution Its photocorrosion suppression. *J. Alloys Compd.* **2018**, *740*, 574–586. [CrossRef]

18. Morales-Torres, S.; Pastrana-Martínez, L.M.; Figueiredo, J.L.; Faria, J.L.; Silva, A.M. Design of graphene-Based TiO$_2$ photocatalysts—A review. *Environ. Sci. Pollut. Res.* **2012**, *19*, 3676–3687. [CrossRef]

19. Morales-Torres, S.; Silva, T.L.S.; Pastrana-Martínez, L.M.; Brandão, A.T.; Figueiredo, J.L.; Silva, A.M. Modification of the surface chemistry of single and multi-Walled carbon nanotubes by HNO$_3$ and H$_2$SO$_4$ hydrothermal oxidation for application in direct contact membrane distillation. *Phys. Chem. Chem. Phys.* **2014**, *16*, 12237–12250. [CrossRef]

20. Liang, D.; Cui, C.; Hub, H.; Wang, Y.; Xu, S.; Ying, B.; Li, P.; Lu, B.; Shen, H. One-Step hydrothermal synthesis of anatase TiO$_2$/reduced graphene oxide nanocomposites with enhanced photocatalytic activity. *J. Alloys Compd.* **2014**, *582*, 236–240. [CrossRef]

21. Zhao, D.; Sheng, G.; Chenab, C.; Wang, X. Enhanced photocatalytic degradation of methylene blue under visible irradiation on graphene@TiO$_2$ dyade structure. *Appl. Catal. B Environ.* **2012**, *111*, 303–308. [CrossRef]

22. Zhao, Y.; Wei, Y.; Wu, X.; Zheng, H.; Zhao, Z.; Liu, J.; Li, J. Graphene-wrapped Pt/TiO$_2$ photocatalysts with enhanced photogenerated charges separation and reactant adsorption for high selective photoreduction of CO$_2$ to CH$_4$. *Appl. Catal. B Environ.* **2018**, *226*, 360–372. [CrossRef]

23. Fattahi, A.; Liang, R.; Kaur, A.; Schneider, O.; Arlos, M.J.; Peng, P.; Servos, M.; Zhou, N. Photocatalytic degradation using TiO$_2$-Graphene nanocomposite under UV-LED illumination: Optimization using response surface methodology. *J. Environ. Chem. Eng.* **2019**, *7*, 103366. [CrossRef]

24. Police, A.K.R.; Chennaiahgari, M.; Boddula, R.; Vattikuti, S.P.; Mandari, K.K.; Chan, B. Single-Step hydrothermal synthesis of wrinkled graphene wrapped TiO2 nanotubes for photocatalytic hydrogen production and supercapacitor applications. *Mater. Res. Bull.* **2018**, *98*, 314–321. [CrossRef]

25. Ashraf, M.A.; Liu, Z.; Peng, W.-X.; Jermsittiparsert, K.; Hosseinzadeh, G.; Hosseinzadeh, R. Combination of sonochemical and freeze-Drying methods for synthesis of graphene/Ag-Doped TiO$_2$ nanocomposite: A strategy to boost the photocatalytic performance via well distribution of nanoparticles between graphene sheets. *Ceram. Int.* **2020**, *46*, 7446–7452. [CrossRef]

26. Wang, X.; Sun, G.; Routh, P.; Kim, Y.-J.; Huang, W.; Chen, P. Heteroatom-Doped graphene materials: Syntheses, properties and applications. *Chem. Soc. Rev.* **2014**, *43*, 7067–7098. [CrossRef]

27. Wang, X.; Li, X.; Zhang, L.; Yoon, Y.; Weber, P.K.; Wang, H.; Guo, J.; Dai, H. N-Doping of Graphene Through Electrothermal Reactions with Ammonia. *Science* **2009**, *324*, 768–771. [CrossRef]

28. Zhang, L.-S.; Liang, X.-Q.; Song, W.; Wu, Z.-Y. Identification of the nitrogen species on N-Doped graphene layers and Pt/NG composite catalyst for direct methanol fuel cell. *Phys. Chem. Chem. Phys.* **2010**, *12*, 12055. [CrossRef]

29. Sheng, Z.-H.; Shao, L.; Chen, J.-J.; Bao, W.-J.; Wang, F.; Xia, X.-H. Catalyst-Free Synthesis of Nitrogen-Doped Graphene via Thermal Annealing Graphite Oxide with Melamine and Its Excellent Electrocatalysis. *ACS Nano* **2011**, *5*, 4350–4358. [CrossRef]

30. Wang, H.; Zhou, Y.; Wu, D.; Liao, L.; Zhao, S.; Peng, H.; Liu, Z. Synthesis of Boron-Doped Graphene Monolayers Using the Sole Solid Feedstock by Chemical Vapor Deposition. *Small* **2013**, *9*, 1316–1320. [CrossRef]

31. Li, R.; Wei, Z.; Gou, X.; Xu, W. Phosphorus-Doped graphene nanosheets as efficient metal-Free oxygen reduction electrocatalysts. *RSC Adv.* **2013**, *3*, 9978. [CrossRef]

32. Yang, Z.; Yao, Z.; Li, G.; Fang, G.; Nie, H.; Liu, Z.; Zhou, X.; Chen, X.; Huang, S. Sulfur-Doped Graphene as an Efficient Metal-free Cathode Catalyst for Oxygen Reduction. *ACS Nano* **2011**, *6*, 205–211. [CrossRef]

33. Poh, H.L.; Šimek, P.; Sofer, Z.; Pumera, M. Sulfur-Doped Graphene via Thermal Exfoliation of Graphite Oxide in H_2S, SO_2, or CS_2 Gas. *ACS Nano* **2013**, *7*, 5262–5272. [CrossRef]

34. Putri, L.K.; Ong, W.-J.; Chang, W.S.; Chai, S.-P. Heteroatom doped graphene in photocatalysis: A review. *Appl. Surf. Sci.* **2015**, *358*, 2–14. [CrossRef]

35. Pedrosa, M.; Da Silva, E.S.; Pastrana-Martínez, L.M.; Drazic, G.; Falaras, P.; Faria, J.L.; Figueiredo, J.L.; Silva, A.M. Hummers' and Brodie's graphene oxides as photocatalysts for phenol degradation. *J. Colloid Interface Sci.* **2020**, *567*, 243–255. [CrossRef]

36. Mou, Z.; Wu, Y.; Sun, J.; Yang, P.; Du, Y.; Lu, C. TiO_2 Nanoparticles-Functionalized N-Doped Graphene with Superior Interfacial Contact and Enhanced Charge Separation for Photocatalytic Hydrogen Generation. *ACS Appl. Mater. Interfaces* **2014**, *6*, 13798–13806. [CrossRef]

37. Pedrosa, M.; Pastrana-Martínez, L.M.; Pereira, M.F.R.; Faria, J.L.; Figueiredo, J.L.; Silva, A.M. N/S-Doped graphene derivatives and TiO_2 for catalytic ozonation and photocatalysis of water pollutants. *Chem. Eng. J.* **2018**, *348*, 888–897. [CrossRef]

38. Gopalakrishnan, K.; Joshi, H.M.; Kumar, P.; Panchakarla, L.; Rao, C. Selectivity in the photocatalytic properties of the composites of TiO2 nanoparticles with B- and N-doped graphenes. *Chem. Phys. Lett.* **2011**, *511*, 304–308. [CrossRef]

39. Albero, J.; Garcia, H. Doped graphenes in catalysis. *J. Mol. Catal. A Chem.* **2015**, *408*, 296–309. [CrossRef]

40. Chowdhury, S.; Jiang, Y.; Muthukaruppan, S.; Balasubramanian, R. Effect of boron doping level on the photocatalytic activity of graphene aerogels. *Carbon* **2018**, *128*, 237–248. [CrossRef]

41. Cai, M.Q.; Su, J.; Zhu, Y.; Wei, X.; Dionysiou, D.D.; Zhang, H.; Dong, C.; Wei, Z. Decolorization of azo dyes Orange G using hydrodynamic cavitation coupled with heterogeneous Fenton process. *Ultrason. SonoChem.* **2016**, *28*, 302–310. [CrossRef]

42. Verma, P.; Samanta, S.K. Microwave-enhanced advanced oxidation processes for the degradation of dyes in water. *Environ. Chem. Lett.* **2018**, *16*, 969–1007. [CrossRef]

43. Tarkwa, J.-B.; Oturan, M.A.; Acayanka, E.; Laminsi, S.; Oturan, M.A. Photo-Fenton oxidation of Orange G azo dye: Process optimization and mineralization mechanism. *Environ. Chem. Lett.* **2018**, *17*, 473–479. [CrossRef]

44. Tekin, D.; Kiziltas, H.; Ungan, H. Kinetic evaluation of ZnO/TiO_2 thin film photocatalyst in photocatalytic degradation of Orange G. *J. Mol. Liq.* **2020**, *306*, 112905. [CrossRef]

45. Hummers, W.S.; Offeman, R.E. Preparation of Graphitic Oxide. *J. Am. Chem. Soc.* **1958**, *80*, 1339. [CrossRef]

46. Fernández-Sáez, N.; Villela-Martinez, D.E.; Carrasco-Marín, F.; Pérez-Cadenas, A.F.; Pastrana-Martínez, L.M. Heteroatom-doped graphene aerogels and carbon-magnetite catalysts for the heterogeneous electro-Fenton degradation of acetaminophen in aqueous solution. *J. Catal.* **2019**, *378*, 68–79. [CrossRef]

47. Ren, X.; Guo, H.; Feng, J.; Si, P.; Zhang, L.; Ci, L. Synergic mechanism of adsorption and metal-free catalysis for phenol degradation by N-doped graphene aerogel. *Chemosphere* **2018**, *191*, 389–399. [CrossRef]

48. Brunauer, S.; Deming, L.S.; Deming, W.E.; Teller, E. On a Theory of the van der Waals Adsorption of Gases. *J. Am. Chem. Soc.* **1940**, *62*, 1723–1732. [CrossRef]

49. Sing, K.S.W. Reporting physisorption data for gas/solid systems with special reference to the determination of surface area and porosity (Recommendations 1984). *Pure Appl. Chem.* **1985**, *57*, 603–619. [CrossRef]

50. Morales-Torres, S.; Pastrana-Martínez, L.M.; Figueiredo, J.L.; Faria, J.L.; Silva, A.M. Graphene oxide-P25 photocatalysts for degradation of diphenhydramine pharmaceutical and methyl orange dye. *Appl. Surf. Sci.* **2013**, *275*, 361–368. [CrossRef]

51. García, M.; Ángeles, F.; Rivera-Utrilla, J.; Bautista-Toledo, I.; Moreno-Castilla, C. Adsorption of Humic Substances on Activated Carbon from Aqueous Solutions and Their Effect on the Removal of Cr(III) Ions. *Langmuir* **1998**, *14*, 1880–1886. [CrossRef]

52. Newcombe, G.; Hayes, R.; Drikas, M. Granular activated carbon: Importance of surface properties in the adsorption of naturally occurring organics. *Colloids Surf. A Physicochem. Eng. Asp.* **1993**, *78*, 65–71. [CrossRef]

53. Silva, C.G.; Faria, J.L. Anatase vs. rutile efficiency on the photocatalytic degradation of clofibric acid under near UV to visible irradiation. *Photochem. Photobiol. Sci.* **2009**, *8*, 705. [CrossRef]

54. Mali, S.S.; Desai, S.K.; Dalavi, D.S.; Betty, C.A.; Bhosale, P.N.; Patil, P.S. CdS-Sensitized TiO$_2$ nanocorals: Hydrothermal synthesis, characterization, application. *Photochem. Photobiol. Sci.* **2011**, *10*, 1652–1658. [CrossRef]

55. Wang, Y.; Ma, C.-L.; Sun, X.-D.; Li, H.-D. Synthesis and characterization of amorphous TiO$_2$ with wormhole-like framework mesostructure. *J. Non-Cryst. Solids* **2003**, *319*, 109–116. [CrossRef]

56. Pastrana-Martínez, L.M.; Morales-Torres, S.; Likodimos, V.; Falaras, P.; Figueiredo, J.L.; Faria, J.L.; Silva, A.M. Role of oxygen functionalities on the synthesis of photocatalytically active graphene–TiO$_2$ composites. *Appl. Catal. B Environ.* **2014**, *158*, 329–340. [CrossRef]

57. Van Khai, T.; Gil Na, H.; Kwak, D.S.; Kwon, Y.J.; Ham, H.; Shim, K.B.; Kim, H.W. Significant enhancement of blue emission and electrical conductivity of N-doped graphene. *J. Mater. Chem.* **2012**, *22*, 17992. [CrossRef]

58. Chen, L.; Cui, X.; Wang, Y.; Wang, M.; Qiu, R.; Shu, Z.; Zhang, L.; Hua, Z.; Cui, F.; Wei, C.; et al. One-Step synthesis of sulfur doped graphene foam for oxygen reduction reactions. *Dalton Trans.* **2014**, *43*, 3420–3423. [CrossRef]

59. Van Khai, T.; Gil Na, H.; Kwak, D.S.; Kwon, Y.J.; Ham, H.; Shim, K.B.; Kim, H.W. Comparison study of structural and optical properties of boron-doped and undoped graphene oxide films. *Chem. Eng. J.* **2012**, *211*, 369–377. [CrossRef]

60. Yang, H.G.; Sun, C.; Qiao, S.; Zou, J.; Liu, G.; Smith, S.C.; Cheng, H.-M.; Lu, G. Anatase TiO$_2$ single crystals with a large percentage of reactive facets. *Nature* **2008**, *453*, 638–641. [CrossRef]

61. Pastrana-Martínez, L.M.; Morales-Torres, S.; Papageorgiou, S.K.; Katsaros, F.; Romanos, G.E.; Figueiredo, J.L.; Faria, J.L.; Falaras, P.; Silva, A.M. Photocatalytic behaviour of nanocarbon–TiO$_2$ composites and immobilization into hollow fibres. *Appl. Catal. B Environ.* **2013**, *142*, 101–111. [CrossRef]

62. Moon, I.K.; Lee, J.; Ruoff, R.S.; Lee, H. Reduced graphene oxide by chemical graphitization. *Nat. Commun.* **2010**, *1*, 1–6. [CrossRef]

63. Fan, W.; Lai, Q.; Zhang, Q.; Wang, Y. Nanocomposites of TiO$_2$ and Reduced Graphene Oxide as Efficient Photocatalysts for Hydrogen Evolution. *J. Phys. Chem. C* **2011**, *115*, 10694–10701. [CrossRef]

64. Lachheb, H.; Puzenat, E.; Houas, A.; Ksibi, M.; Elaloui, E.; Guillard, C.; Herrmann, J.-M. Photocatalytic degradation of various types of dyes (Alizarin S, Crocein Orange G, Methyl Red, Congo Red, Methylene Blue) in water by UV-irradiated titania. *Appl. Catal. B Environ.* **2002**, *39*, 75–90. [CrossRef]

65. Sun, J.; Qiao, L.; Sun, S.-P.; Wang, G. Photocatalytic degradation of Orange G on nitrogen-Doped TiO$_2$ catalysts under visible light and sunlight irradiation. *J. Hazard. Mater.* **2008**, *155*, 312–319. [CrossRef]

66. Banerjee, S.; Pillai, S.C.; Falaras, P.; O'Shea, K.E.; Byrne, J.; Dionysiou, D.D. New Insights into the Mechanism of Visible Light Photocatalysis. *J. Phys. Chem. Lett.* **2014**, *5*, 2543–2554. [CrossRef]

67. Rengifo-Herrera, J.; Pierzchała, K.; Sienkiewicz, A.; Forro, L.; Kiwi, J.; Pulgarin, C. Abatement of organics and Escherichia coli by N, S co-doped TiO2 under UV and visible light. Implications of the formation of singlet oxygen ($^1O_2$) under visible light. *Appl. Catal. B Environ.* **2009**, *88*, 398–406. [CrossRef]

68. Jiang, J.-X.; Zhang, Q.; Li, Y.-H.; Li, L. Three-Dimensional network graphene aerogel for enhancing adsorption and visible light photocatalysis of nitrogen-doped TiO$_2$. *Mater. Lett.* **2019**, *234*, 298–301. [CrossRef]

69. Zhang, Y.; Yang, H.M.; Park, S.-J. Synthesis and characterization of nitrogen-doped TiO$_2$ coatings on reduced graphene oxide for enhancing the visible light photocatalytic activity. *Curr. Appl. Phys.* **2018**, *18*, 163–169. [CrossRef]

70. Munikrishnappa, C.; Kumar, S.; Shivakumara, S.; Rao, G.M.; Munichandraiah, N. The TiO$_2$-Graphene oxide-Hemin ternary hybrid composite material as an efficient heterogeneous catalyst for the degradation of organic contaminants. *J. Sci. Adv. Mater. Devices* **2019**, *4*, 80–88. [CrossRef]

71. Prabhu, S.; Cindrella, L.; Kwon, O.J.; Mohanraju, K. Photoelectrochemical, photocatalytic and photochromic performance of rGO-TiO$_2$WO$_3$ composites. *Mater. Chem. Phys.* **2019**, *224*, 217–228. [CrossRef]

72. Kim, S.-R.; Ali, I.; Kim, J.-O. Effect of synthesis parameters on visible light photocatalytic activity of graphene-TiO$_2$ nanocomposites for industrial wastewater treatment. *J. Ind. Eng. Chem.* **2018**, *66*, 370–380. [CrossRef]

73. Siwińska-Stefańska, K.; Fluder, M.; Tylus, W.; Jesionowski, T. Investigation of amino-Grafted TiO$_2$/reduced graphene oxide hybrids as a novel photocatalyst used for decomposition of selected organic dyes. *J. Environ. Manag.* **2018**, *212*, 395–404. [CrossRef] [PubMed]

74. Zhang, J.-J.; Fang, S.-S.; Mei, J.-Y.; Zheng, G.-P.; Zheng, X.-C.; Guan, X.-X. High-Efficiency removal of rhodamine B dye in water using g-C$_3$N$_4$ and TiO$_2$ co-hybridized 3D graphene aerogel composites. *Sep. Purif. Technol.* **2018**, *194*, 96–103. [CrossRef]